Commun Nonlinear Sci Numer Simulat 26 (2015) 167–183

Contents lists available at ScienceDirect

Commun Nonlinear Sci Numer Simulat

journal homepage: www.elsevier.com/locate/cnsns

Thermal convection in a nonlinear non-Newtonian magnetic fluid

D. Laroze [a,b,c,*], H. Pleiner [b]

[a] Instituto de Alta Investigación, Universidad de Tarapacá, Casilla 7D, Arica, Chile
[b] Max Planck Institute for Polymer Research, D 55021 Mainz, Germany
[c] SUPA School of Physics and Astronomy, University of Glasgow, Glasgow G12 8QQ, United Kingdom

ARTICLE INFO

Article history:
Received 25 February 2014
Received in revised form 12 November 2014
Accepted 5 January 2015
Available online 23 January 2015

Keywords:
Thermal convection
Magnetic fluid
Viscoelastic fluid

ABSTRACT

We report theoretical and numerical results on thermal convection of a magnetic fluid in a viscoelastic carrier liquid. The viscoelastic properties are described by a general nonlinear viscoelastic model that contains as special cases the standard phenomenological constitutive equations for the stress tensor. In order to explore numerically the system we perform a truncated Galerkin expansion obtaining a generalized Lorenz system with ten modes. We find numerically that the system has stationary, periodic and chaotic regimes. We establish phase diagrams to identify the different dynamical regimes as a function of the Rayleigh number and the viscoelastic material parameters.

1. Introduction

Convection in fluids driven by thermal gradients have been at the very origin of the field of nonlinear physics and pattern formation [1]. Very early on, investigations have been extended to e.g. binary mixture, non-Newtonian, and magnetic fluids. In such systems, new channels for dissipating energy (e.g. Soret effect), additional time scales (e.g. stress relaxation) and additional driving forces (e.g. magnetic field) lead to new phenomena at the instability thresholds and the pattern forming processes, above. Among the many examples we mention investigations of thermal convection in non-Newtonian binary mixtures [2–9], in non-Newtonian magnetic fluids [10–14], and in binary magnetic fluids [15,16].

The technological applications of magnetic fluids [17] and their biomedical importance [18–22] is closely related to non-Newtonian properties, which are either magnetic field-induced [23–25] or due to the carrier liquid [26–32] (e.g. in blood [33–35]). In this manuscript we are particularly interested in the interplay of nonlinear non-Newtonian with magnetic properties with respect to thermal convection. Despite the black appearance of most ferrofluids, thermal convection experiments [36–47] are a valuable source to investigate the nonlinear properties of those materials.

To describe the nonlinear non-Newtonian aspects we will use a general hydrodynamic description of nonlinear viscoelasticity (PLB) [48] in terms of a dynamic equation for the (nonlinear) strain tensor. Using the standard hydrodynamic procedure including all symmetry and thermodynamic requirements, one can derive the form of the viscoelastic equations, rather than postulating them phenomenologically. PLB is applicable to arbitrarily large deformations, rotations and flows [49] and contains the solid limit, correctly. It contains as special limits typical visco-elastic models, such as Maxwell, Oldroyd, Giesekus, Leonov and KBKZ [50]. However, it overcomes the drawback of those popular models that use quasi-linear constitutive

* Corresponding author at: Instituto de Alta Investigación, Universidad de Tarapacá, Casilla 7D, Arica, Chile.
E-mail address: dlarozen@uta.cl (D. Laroze).

http://dx.doi.org/10.1016/j.cnsns.2015.01.002
1007-5704/

relations between stress and strain rate tensors. As a result, it is no longer sufficient to restrict ourselves to the second harmonic approximation when the convection problem is solved numerically.

The magnetic aspects of the fluid are taken as those of a non-conducting ferrofluid including magnetic buoyancy, pyromagnetic behavior, and nonlinear magnetization in the magnetostatic limit [15]. The magnetic fluid is considered here as a one-component fluid neglecting all binary mixture effects. We also focus on two dimensional solutions (roll patterns), only. We show that the system can exhibit stationary, periodic, and chaotic regimes depending on the control parameters. The paper is organized as follows: In Section 2, the basic nonlinear hydrodynamic equations for viscoelastic magnetic fluid convection are presented. In Section 3 for two dimensional roll patterns a truncated Galerkin expansion is used to derive a set of coupled nonlinear ordinary differential equations. In Section 4 numerical simulations are performed and the results are explained. Finally, a summary is given in Section 5. Some preliminary results have been presented before at the Nordic Rheology Conference [51].

2. Basic equations

We consider an (infinite) horizontal layer of thickness d of an incompressible magnetic fluid with a viscoelastic carrier liquid in a vertical gravitational field $\mathbf{g}$. We choose the z-axis such that $\mathbf{g} = -g\hat{\mathbf{z}}$ and the layer boundaries are at $z = 0$ and $z = d$. A static temperature difference across the layer is imposed, $T(z = d) = T_0 - \beta d$ and $T(z = 0) = T_0$ with T_0 the ambient temperature without any heating or cooling. We will only consider the case of heating from below, $\beta > 0$. An external magnetic field $\mathbf{H}_0$ is assumed along the vertical direction. The actual magnetic field in the layer, $\mathbf{H}$, would be homogeneous, if the magnetic fluid were absent. The magnetic fluid properties are modeled as those of electrically nonconducting superparamagnets. Within the Boussinesq approximation, the balance equations are

$$\nabla \cdot \mathbf{v} = 0, \tag{1}$$

$$\rho_0 d_t \mathbf{v} = -\nabla p_{eff} - \nabla \cdot \boldsymbol{\sigma} + \rho \mathbf{g} + \mathbf{M} \cdot \nabla \mathbf{H}, \tag{2}$$

$$\frac{c_{v,H}}{T_0} d_t T + \chi_T \mathbf{H}_0 \cdot d_t \mathbf{H} = \kappa \nabla^2 T, \tag{3}$$

where $d_t f = \partial_t f + \mathbf{v} \cdot \nabla f$ is the material derivative, $\mathbf{v}$ the velocity field, p_{eff} the effective pressure, ρ the mass density (and ρ_0 its equilibrium value), $\mathbf{M}$ the magnetization field, $c_{v,H}$ the specific heat capacity at constant volume and magnetic field, χ_T the pyromagnetic coefficient, κ the thermal diffusivity, and χ_H describing the magnetic field dependence of the susceptibility.

Within the Boussinesq approximation, density modulations, $\delta\rho = \rho - \rho_0$ are zero, except when calculating the buoyancy force, where a linear equation of state is used

$$\delta\rho = \rho_0(-\alpha_T \delta T + \alpha_H \mathbf{H}_0 \cdot \delta\mathbf{H}), \tag{4}$$

that describes thermal (α_T) and magnetic (α_H) expansion.

In addition, for the magnetic field $\mathbf{H}$ and the magnetic induction $\mathbf{B}$, static Maxwell equations are imposed

$$\nabla \times \mathbf{H} = \mathbf{0}, \tag{5}$$

$$\nabla \cdot \mathbf{B} = 0 \tag{6}$$

with $\mathbf{B} = \mathbf{H} + \mathbf{M}$. For the magnetic field a scalar magnetic potential $\mathbf{H} = -\nabla\phi$ is used. Modulations of the magnetization field are described by the equation of state

$$\delta\mathbf{M} = \chi_0 \delta\mathbf{H} + \mathbf{H}_0(\chi_T \delta T + \chi_H \mathbf{H}_0 \cdot \delta\mathbf{H}) \tag{7}$$

reflecting the fact that the magnetic susceptibility is a function of temperature and field [52].

2.1. PLB viscoelastic model

In a Newtonian incompressible fluid, the dissipative part of the stress tensor is related to the strain rate tensor via the Newton law, $\boldsymbol{\sigma} = -2\nu\boldsymbol{D}$, where $\boldsymbol{D}$ is the symmetric part of the velocity field gradient and ν is the kinematic viscosity.

For non-Newtonian fluids, an additional dynamic variable, the nonlinear Eulerian strain tensor U_{ij}, is introduced in the PLB model. It satisfies a nonlinear relaxation equation [48]

$$d_t U_{ij} - D_{ij} + U_{ki}\nabla_j v_k + U_{kj}\nabla_i v_k = -\frac{1}{\tau_1} U_{ij} - \frac{1}{\tau_2} U_{ik} U_{jk} \tag{8}$$

with $\{\tau_1, \tau_2\}$ the linear and nonlinear relaxation constants. If these relaxation times diverge, elasticity is permanent, suitable to describe solid matter, while for vanishing relaxation times (and elastic moduli) the behavior of simple fluids is obtained.

Thermodynamics then requires the stress tensor in Eq. (2) to contain elastic as well as viscous (plastic) parts and is written up to quadratic nonlinearities as

$$\sigma_{ij} = -K_1 U_{ij} + K_2 U_{ik} U_{jk} - 2\nu_1 D_{ij} - \nu_2(U_{ik} D_{jk} + U_{jk} D_{ik}), \tag{9}$$

where $\{K_1, K_2, \nu_1, \nu_2\}$ are the linear and nonlinear elastic and viscous constants, respectively. This description can be generalized to even more complex fluids and soft matter systems in a controlled way, since the connection of the dynamic equation for the strain tensor with possible additional degrees of freedom follows standard thermodynamic and hydrodynamic procedures, while the heuristic generalization of the constitutive equation reaches its limits, rapidly. Furthermore, realistic boundary conditions are straightforward for the strain field, but not at all, if the stress is used as variable.

2.2. Boundary conditions and the perturbation of the conduction state

Given the applied temperature gradient, assuming zero velocity and rigid interfaces, using the standard continuity conditions of the Maxwell equations, i.e., $\mathbf{n} \times (\mathbf{H}_{in} - \mathbf{H}_{ex}) = \mathbf{0}$ and $\mathbf{n} \cdot (\mathbf{B}_{in} - \mathbf{B}_{ex}) = 0$, where $\mathbf{n}$ is the unit normal vector of the boundaries, the pure heat conductive, quiescent state is given by

$$\mathbf{v}_{con} = 0, \tag{10}$$

$$\boldsymbol{U}_{con} = 0, \tag{11}$$

$$T_{con}(z) = T_0 - \beta z, \tag{12}$$

$$\mathbf{H}_{con}(z) = \quad \mathbf{H}_0(1 + \lambda\beta z), \tag{13}$$

where $\lambda = \chi_T/(1+\chi)$ with $\chi = \chi_0 + \chi_H H_0^2$.

The next step is to derive the equations for the perturbation from this heat conducting state and to investigate their stability. To do so in dimensionless form we introduce the characteristic scales, d for length, d^2/κ for time, κ/d for velocity, βd for temperature, $\beta d^2 \chi_T/(1+\chi_H)$ for the magnetic scalar potential and $\nu_1\kappa/d^2$ for the pressure and the stress tensor. After some algebra, the dimensionless equations for the perturbations of the dimensionless velocity ($\mathbf{v}$), temperature θ, and magnetic potential ϕ, can be written as

$$\boldsymbol{\nabla} \cdot \mathbf{v} = \mathbf{0}, \tag{14}$$

$$P^{-1} d_t \mathbf{v} = -\boldsymbol{\nabla} p_{eff} - \boldsymbol{\nabla} \cdot \boldsymbol{\sigma} + Ra\boldsymbol{\Sigma}(\theta, \phi), \tag{15}$$

$$d_t(\theta - M_4 \partial_z \phi) = (1 - M_4) v_z + \boldsymbol{\nabla}^2 \theta, \tag{16}$$

$$(\partial_{zz} + M_3[\partial_{xx} + \partial_{yy}])\phi - \partial_z \theta = 0, \tag{17}$$

$$\boldsymbol{\nabla}^2 \phi_{ext} = 0 \tag{18}$$

with the abbreviation $\boldsymbol{\Sigma} \equiv M_1 \theta \boldsymbol{\nabla}(\partial_z \phi) + \hat{\mathbf{z}}([1+M_1]\theta - [M_1 - M_5]\partial_z \phi)$. The perturbation equation for U_{ij} reads

$$d_t U_{ij} - D_{ij} + U_{ki}\boldsymbol{\nabla}_j v_k + U_{kj}\boldsymbol{\nabla}_i v_k = -\frac{1}{\Gamma_1} U_{ij} - \frac{1}{\Gamma_2} U_{ik} U_{jk} \tag{19}$$

with $\Gamma_n = \kappa\tau_n/d^2$ for $n \in \{1, 2\}$. This implies for the stress tensor

$$\sigma_{ij} = -E_1 U_{ij} + E_2 U_{ik} U_{jk} - 2D_{ij} - Z(U_{ik} D_{jk} + U_{jk} D_{ik}) \tag{20}$$

with $E_n = K_n d^2/\nu_1\kappa$ and $Z = \nu_2/\nu_1$. The Newtonian part $\sigma_{ij} \sim -2D_{ij}$ comes without a phenomenological parameter within this normalization.

Eqs. (14)–(20), contain the standard dimensionless numbers of magnetic thermal convection, the Rayleigh number, $Ra = \alpha_T g \beta d^4/\kappa\nu_1$ (buoyancy effect), the Prandtl number, $P = \nu_1/\kappa, M_1 = \beta\chi_T^2 H_0^2/(\rho_0 g \alpha_T(1+\chi))$ (Kelvin force relative to buoyancy force), $M_3 = (1+\chi_0)/(1+\chi) \approx 1 - (\chi_H H_0^2)/(1+\chi_0)$, (nonlinear behavior of the magnetization) and two further magnetic numbers, $M_4 = \chi_T^2 H_0^2 T_0/c_H(1+\chi)$ and $M_5 = \alpha_H \chi_T H_0^2/(\alpha_T(1+\chi))$, which are not related to viscoelastic effects and are commonly neglected due to their smallness [15,16]. The viscoelastic numbers are the relaxation times $\Gamma_{1,2}$, the elastic moduli $E_{1,2}$, and the viscosity ratio Z, which are all positive.

The external driving in $Ra \sim \beta$ and $M_1 \sim H_0^2$ can be varied by several orders of magnitude, while M_3 is typically only slightly larger than 1, $\gtrsim 1$ and only a weak function of the external magnetic field. For P we generally use $P = 10$, suitable for water-based ferrofluids, but in Section 4.6 we discuss in some detail the changes one gets for higher values up to $P \approx 100$. The relaxation times can be varied in viscoelastic ferrofluids quite a bit by either adding a small amount of polymers or applying a magnetic field that leads to chaining. Values up to $\Gamma_1 \sim 1$ seem to be possible, but we show in Section 4.6 that the chaotic behavior is almost independent as long as Γ is between 10^{-6} and 1.

On the linear level ($\Gamma_2 = E_2 = Z = 0$) it is easy to recover the standard (linear) Oldroyd model

$$(1 + \Gamma\partial_t)\sigma_{ij} = (1 + \Lambda\partial_t) D_{ij} \tag{21}$$

with the Deborah number, $\Gamma = \lambda_1\kappa/d^2$, where λ_1 is the stress relaxation time, and the retardation number, $\Lambda = \lambda_2/\lambda_1$, the ratio between the strain rate relaxation time, λ_2, and λ_1. Both descriptions are equivalent with $\Gamma = \Gamma_1$ and

$\Lambda = (1 + E_1\Gamma_1)^{-1}$, revealing however that Λ is restricted by $0 < \Lambda < 1$. The kinematic viscosity ν_1, used to scale the time in the viscoelastic description, is related to the asymptotic viscosity ν_∞ (used in the Oldroyd case) by $\nu_\infty = \nu_1/\Lambda$.

3. Two dimensional system

In this section we study the system of equations using a truncated Galerkin method for a spatially two dimensional case. It is divided into two parts, the first subsection illustrates the full equations, and in the second one the specific Galerkin approximation is exposed.

3.1. Two dimensional equations

For the sake of simplicity, the analysis is limited to two-dimensional flows, $\mathbf{v} = \{-\partial_z\psi, 0, \partial_x\psi\}$ introducing the stream function ψ. In particular, we assume periodicity with wave number k in the lateral direction, x, describing 2-dimensional convection rolls parallel to the y-axis. By the definition and symmetry of U_{ij}, we only have three components in the 2-dimensional case. Finally, the set of equation reduces to

$$P^{-1}d_t\nabla_+^2\psi = Ra([1+M_1]\partial_x\theta - M_1\partial_{xz}\phi) + RaM_1([\partial_x\theta][\partial_{zz}\phi] - [\partial_z\theta][\partial_{xz}\phi]) - \partial_{xz}(\sigma_{zz} - \sigma_{xx}) - \nabla_-^2\,\sigma_{xz}, \tag{22}$$

$$d_t\theta = \partial_x\psi + \nabla_+^2\theta, \tag{23}$$

$$(\partial_{zz} + M_3\partial_{xx})\phi = \partial_z\theta, \tag{24}$$

$$d_tU_{xx} = -\partial_{xz}\psi - 2U_{xz}\partial_{xx}\psi + 2U_{xx}\partial_{xz}\psi - \frac{1}{\Gamma_1}U_{xx} - \frac{1}{\Gamma_2}(U_{xx}^2 + U_{xz}^2), \tag{25}$$

$$d_tU_{xz} = \frac{1}{2}\nabla_-^2\psi + U_{xx}\partial_{zz}\psi - U_{zz}\partial_{xx}\psi - \frac{1}{\Gamma_1}U_{xz} - \frac{1}{\Gamma_2}U_{xz}(U_{xx} + U_{zz}), \tag{26}$$

$$d_tU_{zz} = \partial_{xz}\psi - 2U_{zz}\partial_{xz}\psi + 2U_{xz}\partial_{zz}\psi - \frac{1}{\Gamma_1}U_{zz} - \frac{1}{\Gamma_2}(U_{zz}^2 + U_{xz}^2), \tag{27}$$

where $d_tF = \partial_tF + (\partial_x\psi)(\partial_zF) - (\partial_z\psi)(\partial_xF)$ and $\nabla_\pm^2 = \partial_{xx} \pm \partial_{zz}$. The stress tensor components in term of the strain tensor components are

$$\sigma_{xx} = -E_1U_{xx} + E_2(U_{xx}^2 + U_{xz}^2) + 2\partial_{xz}\psi - Z\Big(U_{xz}\nabla_-^2\psi - 2U_{xx}\partial_{xz}\psi\Big), \tag{28}$$

$$\sigma_{xz} = -E_1U_{xz} + E_2U_{xz}(U_{xx} + U_{zz}) - \partial_{xx}\psi + \partial_{zz}\psi - \frac{1}{2}Z(U_{xx} + U_{zz})\nabla_-^2\psi, \tag{29}$$

$$\sigma_{zz} = -E_1U_{zz} + E_2(U_{xz}^2 + U_{zz}^2) - 2\partial_{xz}\psi - Z\Big(U_{xz}\nabla_-^2\psi + 2U_{zz}\partial_{xz}\psi\Big). \tag{30}$$

We impose idealized thermal and magnetic boundary conditions [12], assume free boundary conditions for the stream function, and vanishing strain tensor components at $z = \{0, 1\}$

$$\theta = \psi = \partial_z^2\psi = \partial_z\phi = U_{xx} = U_{zx} = U_{zz} = 0. \tag{31}$$

Apart from the two dimensional roll pattern considered here, the system could exhibit three dimensional patterns like square or hexagonal ones. To compare their stability range with the roll patterns requires a complete three dimensional analysis, which is well beyond the scope of the present work.

To study this set of equations we perform a Galerkin expansion. For the numerical simulations in the lateral direction we will restrict ourselves to the fundamental mode, neglecting higher harmonics in the x-direction. This assumption can be made since we consider a large container. In the z-direction across the layer a multimode description will be used where necessary. Higher harmonics describe deviations of the variables from the linear regime.

3.2. Galerkin expansion

According to the boundary conditions we can expand the variables as functions of (x, z, t) in the following way [53]

$$\psi = -\frac{1}{k}a_1(t)\sin(\pi z)\sin(kx) + a_2(t)\sin(3\pi z), \tag{32}$$

$$\theta = a_3(t)\sin(\pi z)\cos(kx) + a_4(t)\sin(2\pi z), \tag{33}$$

$$\phi = b_3(t)\sin(\pi z)\cos(kx) + b_4(t)\sin(2\pi z), \tag{34}$$

$$U_{xx} = a_5(t)\sin(\pi z)\sin(kx) + a_6(t)\sin(3\pi z), \tag{35}$$

$$U_{xz} = a_7(t)\sin(\pi z)\sin(kx) + a_8(t)\sin(3\pi z), \tag{36}$$

$$U_{zz} = a_9(t)\sin(\pi z)\sin(kx) + a_10(t)\sin(3\pi z), \tag{37}$$

that fulfills the boundary conditions, automatically. Similar to the Lorenz model, we consider the effect of second harmonics only in the temperature (and consequently in the scalar magnetic potential), with third harmonics in all other variables. The second harmonics of the strain tensor components can be neglected, since they do not modify the dynamics. Indeed, if the third harmonics are absent, the resulting equations are linear and the viscoelastic part decoupled from the rest. Keeping the third harmonics is different from the originally Lorenz model [53] and allows to describe the nonlinear viscoelastic effects.

Substituting the trial functions, Eqs. (32)–(37), into (22)–(27), multiplying these equations by the orthogonal eigenfunctions corresponding to Eqs. (32)–(37), and integrating over a convection cell, $\int_{-\pi/k}^{\pi/k}\int_0^1 dx\,dz$, yields a set of ten ordinary differential equations for the time evolution of the amplitudes, which can written in a vectorial form

$$\dot{\mathbf{X}} = \mathbf{F}(\mathbf{X}, \mathcal{P}), \tag{38}$$

where a dot over a function denotes the scaled time derivative, $\dot{\Pi} = d\Pi/d\tau$, where $\tau = q^2 t$ with $q^2 = k^2 + \pi^2$. The explicit form of Eq. (38) is given in Appendix A. These equations are also functions of the parameters $\mathcal{P} = \{r, M_1, M_2, P, E_1, E_2, \Gamma_1, \Gamma_2, Z\}$, where we have introduced the reduced Rayleigh number $r = Ra/Ra_s$ with Ra_s is the stationary Rayleigh number obtained from linear stability analysis [52]

$$Ra_s = \frac{q^6(k^2 M_3 + \pi^2)}{k^2\left(k^2[1 + M_1]M_3 + \pi^2\right)}. \tag{39}$$

We remark that the equation for the scalar magnetic potential is independent of time and the magnetic amplitudes are slaved and determined by $b_2(t) = -\pi a_2(t)/(k^2 M_3 + \pi^2)$ and $b_3(t) = -a_3(t)/(2\pi)$.

We mention that Eq. (38) correctly contains the limits of ferrofluid convection (no viscoelastic effects) [54] as well as the (linear) Oldroyd fluid convection (no magnetic effects, linearized viscoelastic model) [55–58]. In the next section we analyze numerically model (38) in different dynamical regimes.

4. Numerical results

This section is essentially divided into two parts. In the first subsection we briefly discuss those quantities that are used to characterize spatio-temporal regimes and in the other subsections we present the results of the numerical simulations varying different material parameters.

4.1. Numerical methods

In order to study numerically the dynamical behavior of our system we have integrated Eqs. (A.1)–(A.10) via a classical explicit fourth order Runge–Kutta integration scheme with a fixed time step $\triangle t = 0.01$ guaranteeing a precision of 10^{-8} for the amplitudes. For each set of parameters we let the numerical solution evolve for at least 10^6 time steps in order to exclude transient phenomena. In the plots, where the time dependence of a quantity is shown, we shift the time window to catch the relevant dynamical properties under consideration. This system is a generalization of the Lorenz system, hence we expect that the system can exhibit complex behavior.

In order to investigate how the system changes its dynamical behavior as a function of the parameters involved, we determine bifurcation diagrams. These diagrams are obtained by taking repeatedly the maximum value of the stream function amplitude $X_{1,max}$ in a given time interval for a large range of different values of the parameters. If there is always the same $X_{1,max}$, then the system is constant or periodic, while for a finite continuous distribution of $X_{1,max}$ values, the behavior is either quasi-periodic or chaotic.

In addition, in order to examine in more detail the chaotic regimes as a function of the parameters involved and as a complement to the information from the bifurcation diagrams, we calculate the Lyapunov exponents (LEs), λ_i defined by [59]

$$\lambda_i = \lim_{\tau\to\infty}\frac{1}{\tau}\ln\left(\frac{\|\delta Y_i(\tau)\|}{\|\delta Y_i(0)\|}\right).$$

The LEs are numbers that quantify the distance between two initially close trajectories δY_i of a vector field $\mathbf{Y}$, subject to an evolution equation $dY_i/d\tau = F^i(\mathbf{Y}, \tau)$. For a negative LE this distance vanishes, while for a positive LE it diverges exponentially. The latter is the hallmark of a chaotic behavior [54,59–64]. Our 10-dimensional phase space carries 10 LEs, which can be ordered in descending form, with the largest Lyapunov exponent denoted by λ_{max}. The error Err in the evaluation

of the LEs has been checked by using $Err = \sigma(\lambda_M)/\max(\lambda_M)$, where $\sigma(\lambda_M)$ is the standard deviation of λ_{max}. In all cases studied here Err is of the order of 1%, which is sufficiently small for the purpose of the present analysis.

4.2. Stationary states

The top frame of Fig. 1 shows the normalized stream function amplitude, X_1, as a function of time τ for three different values of the reduced Rayleigh number r. After a transient, X_1 tends to a stationary value, which is zero for $r < 1$ (conduction state) and finite for $r > 1$ (stationary roll state). The saturation amplitude, i.e. $X_{1,sat} = X_1(t \to \infty)$ increases with increasing r and the transient oscillations become longer and more pronounced. The bottom frame shows the saturation amplitude as a function of the magnetic field, $M_1 \sim H_0^2$, in the stationary roll regime, for three different values of M_3. The saturation amplitude increases with a power law $X_{1,sat} \sim M_1^{\xi}$ such that ξ depends on r and the rest of the material parameters. While the magnetic field has a destabilizing effect through M_1 increasing the amplitude, the magnetic nonlinearity M_3 reduces the amplitude, albeit the increase of M_3 is due to an increasing magnetic field. However, the effect of M_1 is dominant.

4.3. Dependence on Rayleigh number

Fig. 2 shows in the upper frame the bifurcation of $X_{1,max}$ as a function of the reduced Rayleigh number r. Stationary states exist, with increasing amplitudes (upper left inset), between $r = 1$ and $r \approx 9$ for the chosen viscoelastic parameters. Above that, the system becomes non-regular, and as the Lyapunov exponents in the lower frame show, also chaotic. There is a window of regular states around between $r \approx 87.5$ and $r \approx 99$, where the chaotic regime is interrupted by a regular, periodic one (lower right inset). A second regular regime is found beyond $r \approx 138$. It is expected that this interplay of regular and non-regular regimes continues when further increasing r.

Figs. 3 and 4 show the system at $r = 13$, which is in the chaotic regime, cf. Fig. 2. The time development of the stream function amplitude is chaotic and, as a consequence, its corresponding Fourier power spectrum is a continuum. Fig. 4 shows the appropriate 3D phase portrait in the form of a strange attractor rather similar to the Lorenz attractor.

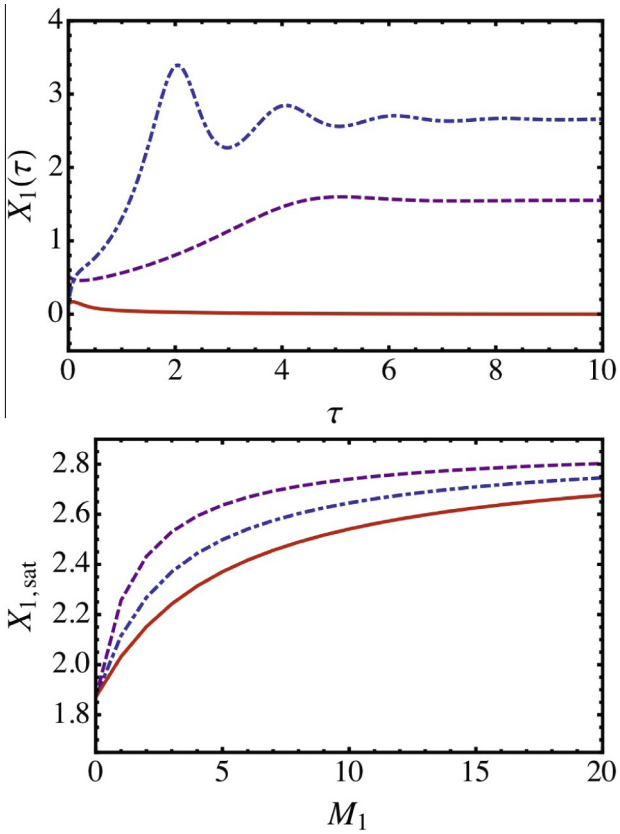

Fig. 1. The stream function amplitude in the stationary regime for three different values of r. The continuous, dashed, and dot-dashed curves are for $r = (0.5, 1.5, 2.5)$, respectively. The top frame shows the time dependence at $M_1 = 10$ and $M_3 = 1.1$. In the bottom frame the saturation value $X_{1,sat} = X_1(\tau \to \infty)|$ is plotted as a function of M_1 for three different values of M_3 at $r = 2.5$. The dashed, dot-dashed, and continuous curves are for $M_3 = (0.5, 1.0, 3.5)$, respectively. The fixed parameters are $k = \pi/\sqrt{2}$, $P = 10$, $E_1 = 10$, $E_2 = 1.5$, $Z = 0.5$, $\Gamma_1 = 0.1$ and $\Gamma_2 = 0.1$.

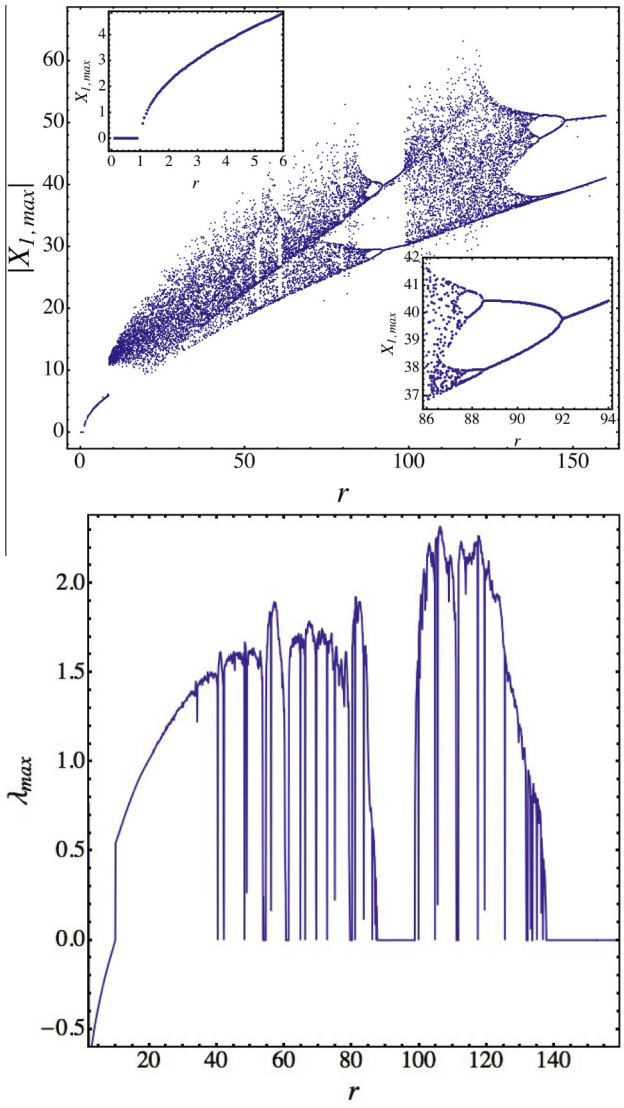

Fig. 2. The bifurcation diagram based on the maxima of the stream function amplitude (upper frame) and the appropriate largest Lyapunov exponent (lower frame) as a function of the reduced Rayleigh number r. The fixed parameters are $k = \pi/\sqrt{2}$, $P = 10$, $M_1 = 10$, $M_3 = 1.1$, $E_1 = 10$, $E_2 = 1.5$, $Z = 0.5$, $\Gamma_1 = 0.1$ and $\Gamma_2 = 0.1$.

Figs. 5 and 6 show the system at $r = 95$ in the first periodic window of the bifurcation diagram Fig. 2. The time dependence of the normalized stream function, X_1 (Fig. 5 top frame) is periodic and the corresponding normalized Fourier power spectrum is discrete. There are multiple peaks in the spectrum, such that the first higher harmonic is the largest peak. Fig. 6 shows a 3D phase portrait of $\{X_1, X_3, X_4\}$ for this state. It can be shown that the shape of this phase portrait is a stable non-symmetric $X_1^2 X_3^2$ orbit in the Sparrow notation [65].

4.4. Dependence on viscoelastic parameters

In order to explore the influence of the viscoelastic parameters, in particular, of the linear (E_1) and nonlinear (E_2) elastic moduli and the nonlinear viscosity (Z) we first considered the state at $r = 13$ that is chaotic for rather small viscoelastic parameters $E_1 = 10$, $E_2 = 1.5$, and $Z = 0.5$. Increasing those numbers to $E_1 = 500$, $E_2 = 100$, and $Z = 3$ a periodic state is found as shown in Figs. 7 and 8. This is a rather simple state as can be seen (Fig. 7) from the time development of the amplitude as well as from the discrete amplitudes in the corresponding Fourier spectrum, where the higher harmonics are less important than first frequency. Apparently, higher elastic moduli tend to suppress chaos. This is even more pronounced in Figs. 9 and 10, where E_1 has been further increased to $E_1 = 800$, and Γ_2 has been also increased to $\Gamma_2 = 10$. Again, a periodic state is found, whose time dependence and Fourier spectrum do not look basically different from those of Fig. 7, but the phase portrait (Fig. 10) reveals a rather different type of periodic state, in the form of a non-symmetric closed orbit.

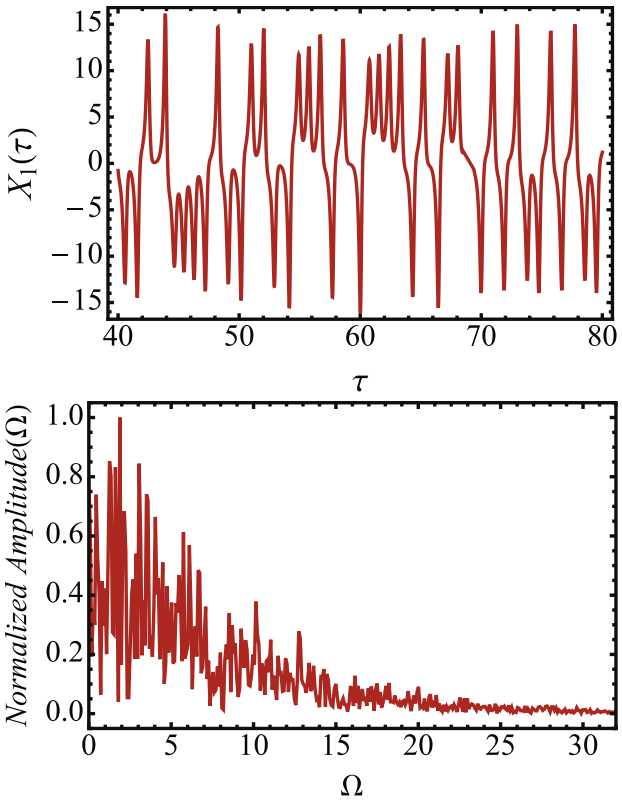

Fig. 3. Amplitudes in a chaotic regime at $r = 13$. At the top the time dependence of X_1 is shown and at the bottom the corresponding normalized Fourier power spectrum is plotted. The fixed parameters are as in Fig. 2.

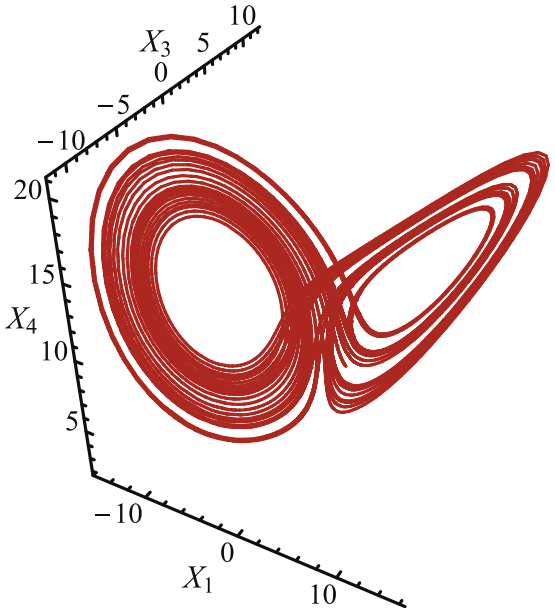

Fig. 4. 3D phase portrait of $\{X_1, X_3, X_4\}$ in the chaotic regime of Fig. 3.

In order to be more systematic, we have calculated first the bifurcation diagram as a function of E_1 in Fig. 11 at a low reduced Rayleigh number $r = 8$ (with the same fixed parameters as in Fig. 2). For low E_1 the system is in the stationary state according to Fig. 2, but beyond a threshold at $E_1 \approx 50$ chaos sets in. Only at much higher values $E_1 \gtrsim 160$ chaos disappears

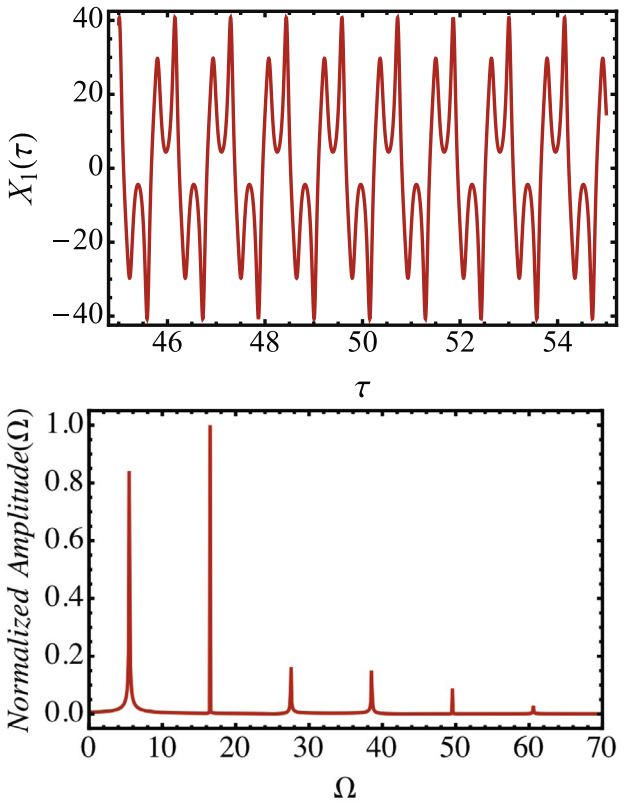

Fig. 5. Amplitudes in a periodic regime at $r = 95$. At the top the time dependence of X_1 is shown and at the bottom the corresponding normalized Fourier power spectrum is plotted. The fixed parameter are as in Fig. 2.

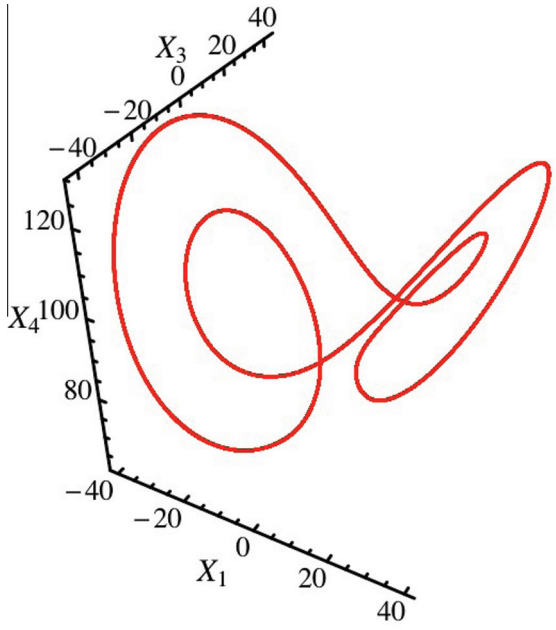

Fig. 6. 3D phase portrait of $\{X_1, X_3, X_4\}$ in the periodic state of Fig. 5.

again and periodic states occur, a few examples of which we have discussed above. It is rather remarkable that increasing the (linear) elastic modulus can trigger chaos in this system, while the suppression of chaos at even higher E_1 (higher internal stiffness) is more intuitive, since obviously, solids cannot show chaotic flow behavior.

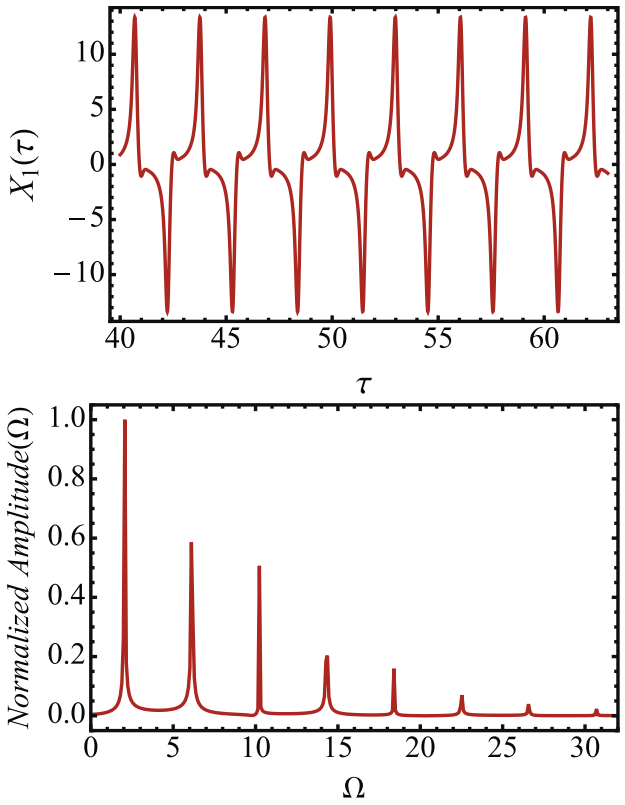

Fig. 7. Amplitudes in a periodic regime at $r = 13$ and higher elastic moduli $E_1 = 500$, $E_2 = 100$, and higher nonlinear viscosity $Z = 3$. All other fixed parameters are as in Fig. 2. At the top the time dependence of X_1 is shown and at the bottom the corresponding Fourier power spectrum is plotted.

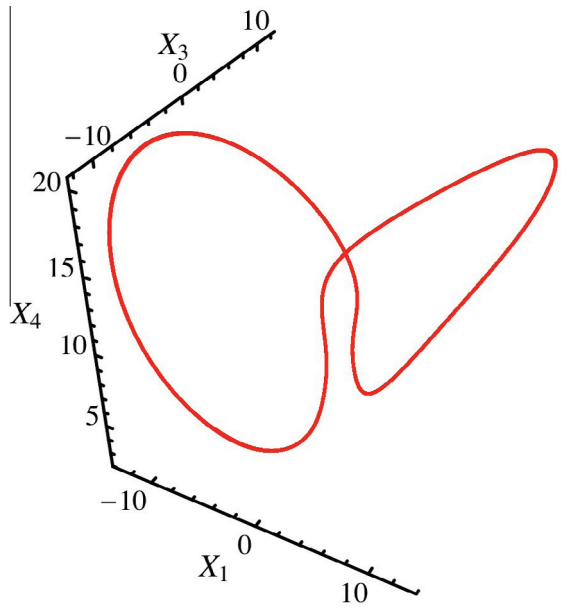

Fig. 8. 3D phase portrait of $\{X_1, X_3, X_4\}$ in the periodic regime of Fig. 7.

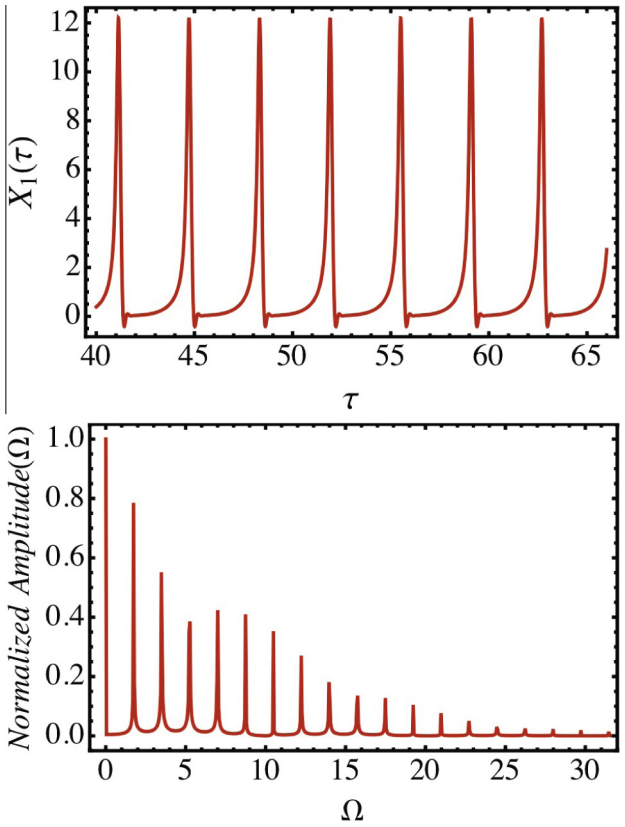

Fig. 9. Amplitudes in a periodic regime at the same $r = 13$, but even higher $E_1 = 800$ and $\Gamma_2 = 10$ compared to Figs. 7 and 8. At the top the time dependence of X_1 is shown and at the bottom the corresponding Fourier power spectrum is plotted. All other fixed parameters are as in Fig. 7.

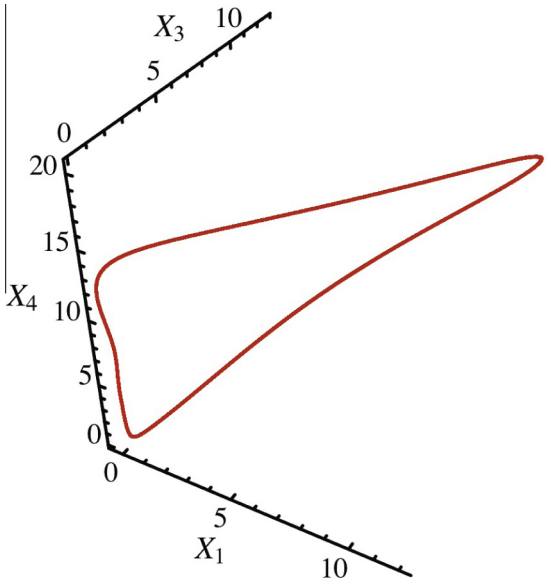

Fig. 10. 3D phase portrait of $\{X_1, X_3, X_4\}$ in the periodic regime of Fig. 9.

Within the range of relaxation times considered here, there is almost no influence on the chaotic behavior. This is demonstrated in Section 4.6 in conjunction with the Prandtl number dependence.

The influence of the nonlinear viscosity Z is shown in another bifurcation diagram in Fig. 12. For intermediate values of $E_1 = 100$ at a small $r = 8$ the system shows chaotic states for low Z values, in accordance with the previous E_1 bifurcation

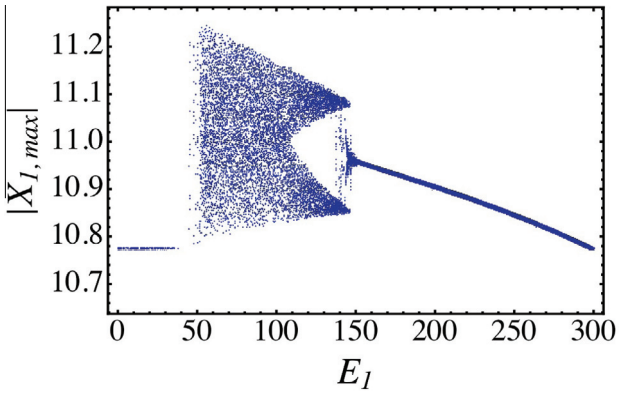

Fig. 11. The bifurcation diagram of X_1 as a function of E_1 at $r = 8$; all other fixed parameters are as in Fig. 2.

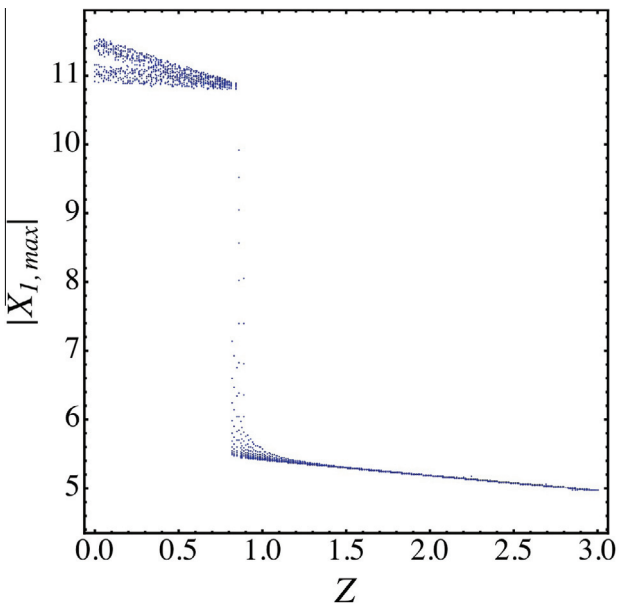

Fig. 12. The bifurcation diagram of X_1 as a function of Z at $E_1 = 100$. The other fixed parameters are as in Fig. 11.

diagram. However, above a sharp transition at $Z \approx 0.7$ the states finally become periodic. This suppression of chaos by a high nonlinear viscosity cannot easily be understood, intuitively.

4.5. Dependence on magnetic parameters

We discuss the largest Lyapunov exponent as a function of both, M_1 and M_3 in Fig. 13. At intermediate elasticity and viscosity parameters, $E_1 = 100$, $E_2 = 10$ and $Z = 3$, and a low $r = 10$ the LEs increase when M_1 or M_3, or both, are increased. For very low values of the magnetic numbers the system is in the stationary regime. However, in contrast to the stationary state, in which M_3 has a stabilizing effect (Fig. 1), chaos is promoted and corroborated by both, M_1 and M_3. The critical value for M_1, where chaos sets in, decreases with increasing M_3, and vice versa.

4.6. Dependence on Prandtl number

Fig. 14 shows the largest Lyapunov exponent λ_{max} as a function P for different values of r. In the top frame we fix the relaxation times to $\Gamma = 10^{-4}$ and in the bottom frame to $\Gamma = 10^{-6}$. Obviously, the onset of chaos is shifted to higher values of the Rayleigh number r, if the Prandtl number is increased. This is independent of the relaxation times, only the numerical noise is stronger for the lower Γ value. In Fig. 15 we analyze the case of a high Prandtl number ($P = 100$) in more detail. One can

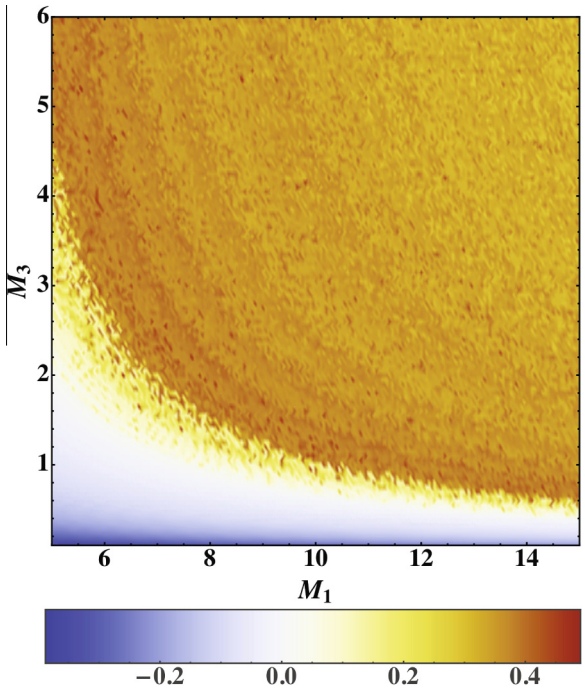

Fig. 13. Phase diagram displaying the largest Lyapunov exponent λ_{max} color coded as a function of both magnetic numbers M_1 and M_3 at $r = 10$ and intermediate viscoelastic parameters $E_1 = 100,\ E_2 = 10$, and $Z = 3$; all other fixed parameters are as in Fig. 2.

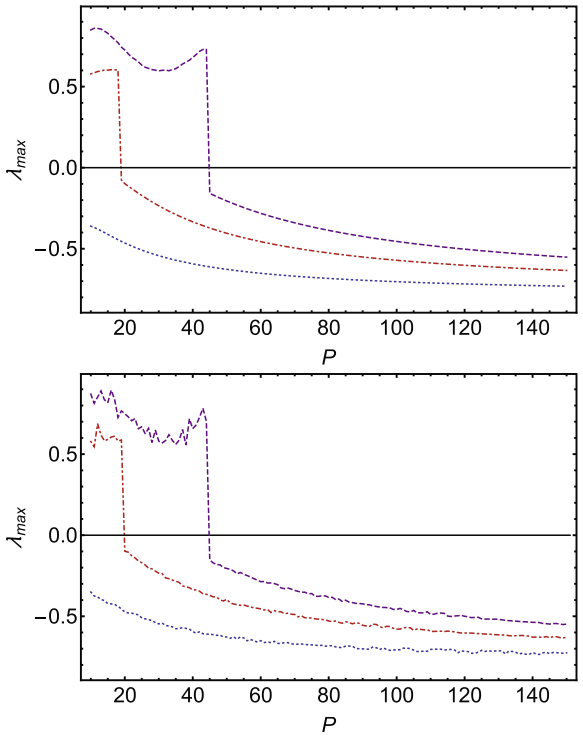

Fig. 14. Largest Lyapunov exponent λ_{max} as a function of Prandtl number, P, for different values of r at $\Gamma_1 = \Gamma_2 = 10^{-4}$ (top) and $\Gamma_1 = \Gamma_2 = 10^{-6}$ (bottom). The dotted, dot-dashed and dashed curves are for $r = (5, 10, 15)$, respectively. The fixed parameters are: $k = \pi/\sqrt{2},\ M_1 = 10,\ M_3 = 1.1,\ E_1 = 10,\ E_2 = 1.5$ and $Z = 0.5$.

observe that not only is the onset to chaos shifted to a rather high value of r, also the route to chaos is different than for low Prandtl numbers: There is now a large periodic state (about $40 < r < 100$) between the stationary state and the chaotic one. These findings are corroborated from a different point of view in Fig. 16, where for an intermediate value of $r = 15$ there is no chaos for $P = 100$ and 50, in contrast to the case of low Prandtl number $P = 10$. For this parameter set it is also obvious that the relaxation times Γ do not play a role within the considered range.

Finally, we remark that for the very small values of Γ_j considered here, we have used a smaller time step ($dt = 10^{-7}$) in the simulations than before, in order to obtain the same error in the Lyapunov exponent as in the previous simulations.

5. Final remarks

In the present work, Rayleigh–Bénard convection in a magnetic viscoelastic liquid is studied. For the viscoelastic properties the PLB model [48] is used. Similar to the Lorenz approach [53], a set of ten coupled non-linear ordinary differential equations is obtained that contains two magnetic and five viscoelastic numbers. The rather large number of relevant dynamic equations is a consequence of the nonlinear viscoelastic description that requires to go beyond the harmonic approximation in the mode analysis. The sequence of different states is obtained by calculating bifurcation diagrams and the largest Lyapunov exponents. Some exemplified states are characterized by the time development of the stream function amplitude and its Fourier spectrum, as well as by phase portraits in a reduced phase space (Lorenz-type attractors, homoclinic orbits, etc.).

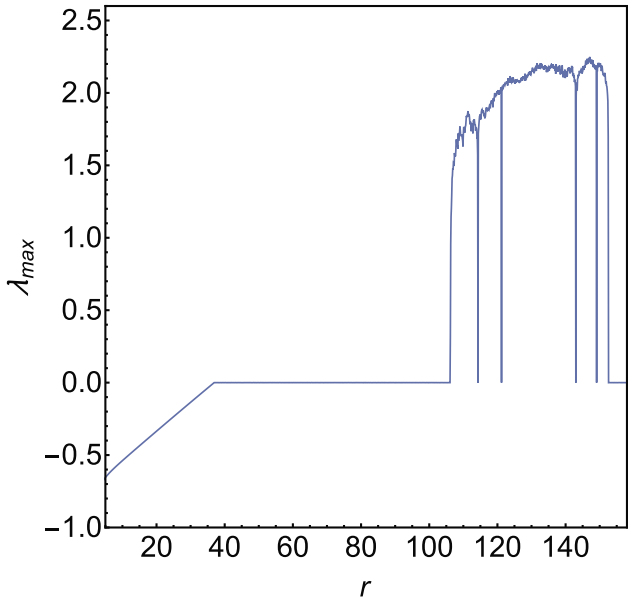

Fig. 15. Largest Lyapunov exponent λ_{max} as a function of r at $P = 100$. The other fixed parameters are the same of Fig. 2.

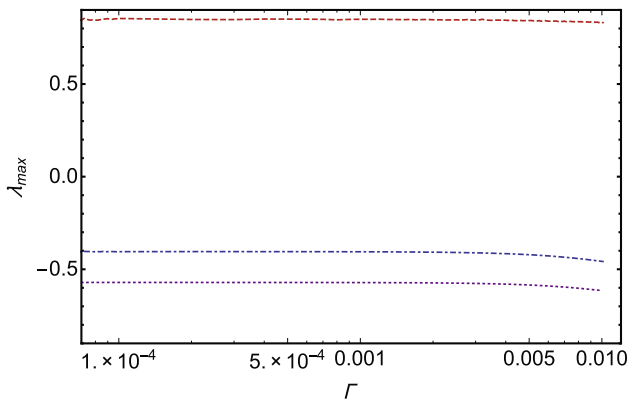

Fig. 16. Largest Lyapunov exponent λ_{max} as a function of $\Gamma = \Gamma_1 = \Gamma_2$ for different values of P at $r = 15$. The dotted, dot-dashed and dashed curves are for $P = (100, 50, 10)$, respectively. The other fixed parameters are the same of Fig. 14.

The stationary bifurcation at low Rayleigh numbers is slightly influenced by the magnetic properties of the fluid, but not at all by the viscoelastic ones. Increasing the Rayleigh number (at rather moderate magnetic and viscoelastic numbers) the system becomes chaotic. The large chaotic regime is interrupted by a window of regular periodic states, before chaos recurs at even higher Rayleigh numbers. Fixing the Rayleigh number at a low value, where a Newtonian fluid is in the stationary regime, chaos is triggered by increasing the elastic number. However, at very large elastic numbers chaos is suppressed and gives rise to regular periodic states. These periodic states are rather different from those at high Rayleigh numbers. It is also shown that high nonlinear viscosity numbers suppress chaos. At intermediate viscoelastic parameters, both magnetic numbers support and increase chaos.

For higher Prandtl numbers chaos is suppressed and requires higher Rayleigh numbers. In addition, there is a periodic state in between the stationary and the chaotic one, and this picture is not changed within a wide range of relaxation times.

Acknowledgments

We acknowledge partial financial support from FONDECYT 11080229; D.L. also from Basal Program Center for Development of Nanoscience and Nanotechnology (CEDENNA), Millennium Scientific Initiative, *P*10-061-*F*, UTA-project 8750-12 and EPSRC under Grant EP/L002922/1.

Appendix A. Generalized Lorenz equations

In this appendix we list the generalized Lorenz Eq. (38) in detailed form

$$\dot{X}_1 = P(X_3 - X_1) - \frac{4\sqrt{2}E_2kP\Sigma}{15q^6}(X_5X_8 + X_6X_7) - \frac{4\sqrt{2}E_2kP\Sigma}{15q^6}(X_8X_9 + X_{10}X_7) + \frac{M_{13}P}{\pi r}X_3X_4 + \frac{6\sqrt{2}\pi^2kP\Sigma Z}{5q^6}(X_2X_5 + X_2X_9) + \frac{4K^4PZ}{15\pi q^4}(X_1X_{10} + X_1X_6) - \frac{\pi E_1kP\Sigma}{\sqrt{2}q^6}X_7, \tag{A.1}$$

$$\dot{X}_2 = -\frac{9\pi^2P}{q^2}X_2 - \frac{E_1P}{q^2}X_8 + \frac{8E_2P}{9\pi q^2}(X_8X_{10} + X_8X_6) - \frac{4E_2P}{15\pi q^2}(X_7X_5 + X_7X_9) + \frac{2\sqrt{2}P\Sigma Z}{15\pi^2k}(X_1X_5 + X_1X_9) - \frac{4\pi PZ}{q^2}(X_2X_6 + X_2X_{10}), \tag{A.2}$$

$$\dot{X}_3 = -X_3 + (r - X_4)X_1, \tag{A.3}$$

$$\dot{X}_4 = -\frac{4\pi^2}{q^2}X_4 + X_1X_3, \tag{A.4}$$

$$\dot{X}_5 = -\frac{X_5}{\Gamma_1} + \frac{16\sqrt{2}kq^2}{15\pi^2}X_1X_8 + \frac{16}{15\pi\Gamma_2}(X_5X_6 + X_7X_8), \tag{A.5}$$

$$\dot{X}_6 = -\frac{X_6}{\Gamma_1} + \frac{8\sqrt{2}kq^2}{15\pi^2}X_1X_7 + \frac{4}{15\pi\Gamma_2}\left(X_5^2 - X_7^2\right) - \frac{8}{9\pi\Gamma_2}\left(X_6^2 - X_8^2\right), \tag{A.6}$$

$$\dot{X}_7 = -\frac{X_7}{\Gamma_1} + \frac{\Sigma q^2}{\sqrt{2}\pi k}X_1 + \frac{8}{15\pi\Gamma_2}(X_{10}X_7 + X_5X_8) + \frac{8}{15\pi\Gamma_2}(X_6X_7 + X_8X_9) + \frac{8\sqrt{2}q^2}{15}\left(\frac{k}{\pi^2}X_1X_{10} - \frac{1}{k}X_1X_6\right) + \frac{24}{5}\pi X_2X_5, \tag{A.7}$$

$$\dot{X}_8 = -\frac{X_8}{\Gamma_1} + \frac{9}{2}\pi^2X_2 - \frac{8}{9\pi\Gamma_2}(X_{10}X_8 + X_6X_8) + \frac{4}{15\pi\Gamma_2}(X_5X_7 + X_7X_9) + \frac{4\sqrt{2}q^2}{15}\left(\frac{k}{\pi^2}X_1X_9 - \frac{1}{k}X_1X_5\right) - 8\pi X_2X_6, \tag{A.8}$$

$$\dot{X}_9 = -\frac{X_9}{\Gamma_1} - \frac{16\sqrt{2}q^2X_1X_8}{15k} + \frac{16}{15\pi\Gamma_2}(X_5X_6 + X_7X_8) + \frac{48\pi}{5}X_2X_7, \tag{A.9}$$

$$\dot{X}_{10} = -\frac{X_{10}}{\Gamma_1} - \frac{8\sqrt{2}q^2X_1X_7}{15k} + \frac{4}{15\pi\Gamma_2}(X_5^2 + X_7^2) - \frac{8}{9\pi\Gamma_2}(X_6^2 + X_8^2) - 16\pi X_2X_8. \tag{A.10}$$

The dot over a function denotes the time derivative, $\dot{\Pi} = d\Pi/d\tau$, with $\tau = q^2t$, such that $q^2 = \pi^2 + k^2$. The new amplitudes, $\{X_j\}$, are related with the old amplitudes, $\{a_j\}$, as follow: $a_1 = (q^2\sqrt{2}/\pi)X_1$, $a_3 = -(\sqrt{2}/(\pi r))X_3$, $a_4 = -X_4/(\pi r)$, and $a_j = X_j$ in

the other cases. Here $M_{13} = \pi k^2 M_1 M_3/(\pi^2 + k^2[1 + M_1]M_3)$, $\Sigma = k^2 - \pi^2$, $K^4 = k^4 - 16\pi^2 k^2 + \pi^4$ and $r = Ra/Ra_s$ with Ra_s given in Eq. (39).

Note that when the viscoelastic effects are neglected, $E_1 = E_2 = Z = 0$ and $\Gamma_1 = \Gamma_2 \to \infty$, we recover the generalized Lorenz model for ferrofluid [54]; which in the nonmagnetic limit reproduces the Lorenz equation [53]. The magnetic effects in Eq. (A.1) are introduced in the terms X_3X_4, the last one being a pure magnetic contribution. Also, in Eq. (A.1) the term X_7 is related to the linear elasticity, while the terms X_5X_8, X_6X_7, X_8X_9 and $X_{10}X_7$ are related to the nonlinear elastic modulus, E_2, and the terms X_1X_{10}, X_1X_6, X_5X_2 and X_9X_2 are related to the nonlinear viscoelastic effect, Z. Eq. (A.2) contains pure higher harmonic combinations, even the linear term since the first is a self-one,X_2, and the second linear term proportional to X_8 is third harmonic of U_{zx}. Eqs. (A.3) and (A.4) are the equations for the temperature amplitudes and they have the same form as in the Lorenz model [53]. Eqs. (A.5)–(A.10) give amplitudes of the strain tensor dynamics. In all these equations the first linear term is connected to the dimensionless relaxation time Γ_1.

References

[1] Cross MC, Hohenberg PC. Rev Mod Phys 1993;65:851.
[2] Kolodner P. J Non-Newtonian Fluid Mech 1998;75:167.
[3] Martinez-Mardones J, Tiemann R, Walgraef D. J Non-Newtonian Fluid Mech 2000;93:1.
[4] Laroze D, Martinez-Mardones J, Perez-Garcia C. Int J Bifurcation Chaos 2005;15:3329.
[5] Wang S, Tan WC. Phys Lett A 2008;372:3046.
[6] Awad FG, Sibanda Sandile P, Motsa S. Appl Math Modell 2010;34:3509.
[7] Kumar A, Bhadauria BS. Phys Fluids 2011;23:054101.
[8] Wang S, Tan WC. Int J Heat Fluid Flow 2011;32:88.
[9] Delenda N, Hirata SC, Ouarzazi MN. J Non-Newtonian Fluid Mech 2012;181–182:11.
[10] Laroze D, Martinez-Mardones J, Pérez LM. Int J Bifurcation Chaos 2010;20:235.
[11] Laroze D, Martinez-Mardones J, Pérez LM, Rojas RG, Mag J. Mag Mat 2010;322:3576.
[12] Pérez LM, Bragard J, Laroze D, Martinez-Mardones J, Pleiner H. J Mag Mag Mat 2011;323:323.
[13] Laroze D, Pérez LM, Bragard J, Cordaro EG, Martinez-Mardones J. Magnetohydrodynamics 2011;47:159.
[14] Laroze D, Martinez-Mardones J, Pleiner H. Eur Phys J Spec Top 2013;219:71.
[15] Ryskin A, Pleiner H. Phys Rev E 2004;69:046301.
[16] Laroze D, Martinez-Mardones J, Bragard J, Vargas P. Physica A 2006;371:46.
[17] Berkovsky BM, Medvdev VF, Krakov MS. The magnetic fluids, engineering application. Oxford: Oxford University Press; 1973.
[18] Mahmoudi M et al. J Phys Chem C 2009;113:2322.
[19] Kim EH, Ahn Y, Lee HS. J Alloys Compd 2007;434:633.
[20] Alexiou C et al. J Drug Targeting 2003;11:139.
[21] Alexiou C et al. J Magn Magn Mater 2002;252:363.
[22] Alexiou C et al. Cancer Res 2000;60:6641.
[23] Yu Borin D, Odenbach S. J Phys: Condens Matter 2009;21:246002.
[24] Lira SA, Miranda JA. Phys Rev E 2009;80:046313.
[25] Lira SA, Miranda JA. Phys Rev E 2009;79:046303.
[26] de Gans BJ, Blom C, Philipse AP, Mellema J. Phys Rev E 1999;60:4518.
[27] Odenbach S, Mag J. Mag Mat 1999;201:149.
[28] Müller HW, Liu M. Phys Rev E 2001;64:061405.
[29] Odenbach S. J Phys: Condens Matter 2004;16:R1135.
[30] Ilg P, Kröger M, Hess S. Phys Rev E 2005;71:031205.
[31] Müller O, Hahn D, Liu M. J Phys: Condens Matter 2006;18:S2623.
[32] Shahnazian H et al. J Phys D: Appl Phys 2009;42:205004.
[33] Popel AS, Johnson PC. Annu Rev Fluid Mech 2005;37:43.
[34] Baskurt OK, Meiselman HJ. Semin Throm Hemost 2003;29:435.
[35] Bishop JJ. Biorheology 2001;38:263.
[36] Braithwaite D, Beaugnon E, Tournier R. Nature 1991;354:134.
[37] Odenbach S. Phys Fluids 1994;6:2535.
[38] Odenbach S, Schwahn D, Stierstadt K. Z Phys B 1995;96:567.
[39] Odenbach S. J Magn Magn Mater 1995;149:155.
[40] Yamaguchi H, Kobori I, Uehata Y, Shimada K. J Magn Magn Mater 1999;201:264.
[41] Odenbach S. J Phys: Condens Matter 2003;15:S1497.
[42] Odenbach S, VŽlker Th. J Magn Magn Mater 2005;289:122.
[43] Engler H, Odenbach S. J Phys: Condens Matter 2008;20:204135.
[44] Bednarz T, Lei C, Patterson JC. Int Commun Heat Mass Trans 2009;36:97.
[45] Bednarz T, Patterson JC, Lei C, Ozoe H. Int Commun Heat Mass Trans 2009;36:781.
[46] Bozhko A, Putin G. Microgravity Sci Technol 2009;21:89.
[47] Lajvardi M, Moghimi-Rad J, Hadi I, Gavili A, Dallali Isfahani T, Zabihi F, et al. J Magn Magn Mater 2010;322:3508.
[48] Pleiner H, Liu M, Brand HR. Rheol Acta 2004;43:502. and references therein.
[49] Müller O. [Ph.D. thesis]. University Tübingen; 2006.
[50] Pleiner H, Liu M, Brand HR. In: Calderer M-C, Terentjev E, editors. IMA volume in mathematics and its applications. Modeling of soft matter, vol. 141. Springer; 2005. p. 99.
[51] Laroze D, Pleiner H. In: Proceedings of the 22nd nordic rheology conference, Copenhagen 2013, Annu Trans Nordic Rheol Soc, vol. 21; 2013. p. 35.
[52] Finlayson BA. J Fluid Mech 1970;40:753.
[53] Lorenz EN. J Atmos Sci 1963;20:130.
[54] Laroze D, Siddheshwar PG, Pleiner H. Commun Nonlinear Sci Numer Simul 2013;18:2436.
[55] Khayat RE. J Non-Newtonian Fluid Mech 1994;53:227.
[56] Khayat RE. Phys Rev E 1995;51:380.
[57] Khayat RE. J Non-Newtonian Fluid Mech 1995;58:331.
[58] Abu-Ramadan E, Hay JM, Khayat RE. J Non-Newtonian Fluid Mech 2003;115:79.
[59] Wolf A, Swift JB, Swinney HL, Vastano JA. Physica D 1985;16:285.

[60] Bonatto C, Gallas JAC. Phys Rev E 2007;75:055204(R);
Bonatto C, Gallas JAC. Philos Trans R Soc A 2008;366:505;
Bonatto C, Gallas JAC, Ueda Y. Phys Rev E 2008;77:026217;
Bonatto C, Gallas JAC. Phys Rev Lett 2008;101:054101.
[61] Laroze D, Bragard J, Suarez OJ, Pleiner H. IEEE Trans Mag 2011;47:3032.
[62] Bragard J, Pleiner H, Suarez OJ, Vargas P, Gallas JAC, Laroze D. Phys Rev E 2011;84:037202.
[63] Laroze D, Becerra-Alonso D, Gallas JAC, Pleiner H. IEEE Trans Mag 2012;48:3567.
[64] Pérez LM, Suarez OJ, Laroze D, Mancini HL. Cent Eur J Phys 2013;11:1629.
[65] Sparrow C. The Lorenz equations: bifurcations, chaos, and strange attractors. Berlin: Springer; 1982.